Elastic scattering of high-energy electrons by dopant atoms within a crystal in transmission electron microscopy

B. G. Mendis

SuperSTEM, Daresbury Laboratory, Keckwick Lane, Daresbury WA4 4AD, UK, and Department of Physics and Astronomy, University of Glasgow, Glasgow G12 8QQ, UK. Correspondence e-mail: b.mendis@physics.gla.ac.uk

A Bloch-wave model of dopant-atom scattering is developed using perturbation theory for parallel illumination in a transmission electron microscope. Dopant-atom scattering causes a change in the Bloch-wave excitations, with transitions from one Bloch state to another being governed by the amplitudes of the Bloch states at the dopant-atom position. The scattering mechanisms therefore depend on whether the dopant atom is substitutional or interstitial as well as the orientation of the crystal. The model is used to calculate the electron wavefunction for substitutional and interstitial Mo atoms in [111]- and [001]-oriented body-centred cubic Fe and the results overall are consistent with multislice simulations. However, subtle differences are also observed. For example, in the Bloch-wave model the phase change of the incident electrons (with respect to the perfect crystal) due to dopant-atom scattering varies with the crystallographic orientation while in multislice theory the phase change is constant. This is likely to be due to the assumptions made in the Bloch-wave model, such as neglect of elastic diffuse scattering. Apart from providing a fundamental understanding of dopant-atom scattering, the model can also potentially be extended to analyse dopant-atom imaging in a scanning transmission electron microscope.

1. Introduction

The distribution of dopant atoms has an important role in optimizing the performance of semiconductor devices (Voyles *et al.*, 2002, 2003, 2004; van Benthem *et al.*, 2005; Allen *et al.*, 2008) and catalysts (Nellist & Pennycook, 1996; Shannon *et al.*, 2007), as well as in grain-boundary engineering (Shibata *et al.*, 2004). In all of the above citations, high-angle annular dark field (HAADF) microscopy in a scanning transmission electron microscope (STEM) was used to image dopant atoms with large atomic number. High-resolution electron microscopy (HREM) has also had some success in this area. Examples include Gd atoms in metallofullerene molecules (Suenaga *et al.*, 2000) as well as oxygen vacancies in perovskite structures and high-T_c YBCO superconductors (Jia *et al.*, 2003). Site occupancies of dopant atoms can also be deduced analytically through techniques such as atom location by channelling-enhanced microanalysis (ALCHEMI) (Spence & Taftø, 1983; Jones, 2002; Sarosi *et al.*, 2003; Mendis & Hemker, 2007). As single-atom detection becomes ever more feasible, it is important to better understand the scattering mechanism(s) of the incident high-energy electrons by the atom of interest.

Traditionally, the effect of dopant atoms on the transmitted electron wavefunction has been simulated using the physical-optics-based multislice algorithm (Voyles *et al.*, 2004; Shannon *et al.*, 2007; Cowley & Moodie, 1957; Kirkland, 1998; Loane *et al.*, 1988). This method is applicable to perfect crystals as well as supercells containing defects, dopant atoms *etc.*, but does not readily provide insight into the fundamental electron-scattering mechanisms. Alternatively, the Bloch-wave method (Hirsch *et al.*, 1965) decomposes the electron wavefunction into components that have a direct relationship with the underlying symmetry of the crystal and provides an intuitive understanding of electron beam–specimen interactions. Bloch waves are more suitable for perfect crystals but can be applied to imperfect crystals containing slowly varying elastic strain fields using the Howie–Whelan equation within the column approximation (Hirsch *et al.*, 1965; Mendis & Hemker, 2008). However, the Howie–Whelan equation is not applicable to electron scattering from a dopant atom where the perturbing force is the change in local electrostatic potential rather than strain. Since scattering from a single dopant atom is weak when compared to all other host atoms within the crystal, the Bloch waves for the imperfect crystal must be similar to those of the perfect crystal without the dopant atom. The wavefunction of the imperfect crystal can therefore be determined from the Bloch-wave solutions for the perfect crystal using standard quantum-mechanical perturbation theories (Bohm, 1951).

The aim of this paper is to develop a Bloch-wave perturbation theory that captures the physics of electron scattering by dopant atoms. Perturbation theory has been used before in Bloch-wave calculations [see, for example, references in Spence & Zuo (1992) as well as Wilkens (1964) and Howie & Basinski (1968)]. In particular, a result similar to equation (9) (see §2.1), which is the key finding of the present study, can be found in the paper by Howie & Basinski (1968). The theory developed in this paper assumes parallel illumination but is easily extended to STEM imaging by treating each partial plane wave within the electron probe individually. The predictions of this model are compared with the Howie–Whelan equation where scattering is due entirely to elastic strain. Numerical examples of scattering from a single Mo atom in body-centred cubic (b.c.c.) Fe in [111] and [001] orientations are then presented. Simulations are carried out for an Mo atom placed at the octahedral interstitial site of the b.c.c. lattice as well as at substitutional positions. Finally, the numerical results are qualitatively compared with multislice simulations to test the accuracy of the perturbation model.

2. Elastic scattering from dopant atoms

2.1. Perturbation theory

Let the incident electrons have wavevector components (k_x, k_y, k_z) with the z axis/xy plane being parallel/perpendicular to the optic axis. The electron wavefunction ψ in the crystal is governed by the steady-state Schrödinger equation (Hirsch *et al.*, 1965):

$$-\left[\frac{h^2}{8\pi^2 m}\nabla^2 + eV(x, y, z)\right]\psi = E\psi, \quad (1)$$

where V and E are the crystal potential and electron energy, respectively, h is Planck's constant, e is the magnitude of the charge of an electron and m is its relativistic mass. The energy E is given by

$$E = (h^2/2m)(k_x^2 + k_y^2 + k_z^2). \quad (2)$$

For high-energy electrons, the longitudinal component of the wavevector undergoes very little change within the crystal and hence the wavefunction ψ can be expanded as (Kirkland, 1998; Cowley, 1988)

$$\psi(x, y, z) = \varphi(x, y, z)\exp(2\pi i k_z z), \quad (3)$$

where the exponential term represents propagation of the electron in vacuum and $\varphi(x, y, z)$ represents the effect of the crystal on the final wavefunction ψ. Substituting equation (3) in (1) gives (after neglecting the $\partial^2\varphi/\partial z^2$ term) (Kirkland, 1998; Cowley, 1988)

$$\frac{\partial\varphi}{\partial z} = i\left\{\left[\frac{\nabla_{xy}^2}{4\pi k_z} + \frac{\pi}{k_z}\left(k_x^2 + k_y^2\right)\right] + \frac{2\pi me}{h^2 k_z}V\right\}\varphi$$

$$\text{where } \nabla_{xy}^2 = \frac{\partial^2}{\partial x^2} + \frac{\partial^2}{\partial y^2}. \quad (4)$$

In a periodic crystal the potential V is expressed as a Fourier series over all reciprocal-lattice vectors (Hirsch *et al.*, 1965). In many cases the more important reciprocal vectors all lie in the zero-order Laue zone (ZOLZ) plane (Spence & Zuo, 1992). This is the so-called projection approximation and is valid for small unit cells and for high-energy electrons with a flat Ewald sphere. Within the projection approximation φ can be shown to be (Hirsch *et al.*, 1965)

$$\varphi(x, y, z) = b(x, y)\exp(2\pi i\gamma z), \quad (5)$$

where γ represents the change in the electron longitudinal wavevector component due to channelling and $b(x, y)$ is the projection of the wavefunction in the xy plane (Hirsch *et al.*, 1965). Equation (5) represents the Bloch-wave solutions for a perfect crystal.

Consider the effect of adding a dopant atom to an otherwise perfect crystal. It is assumed that the dopant atom has a different atomic number, and hence electrostatic potential, to the host atoms but produces negligible strain in the crystal lattice. The potential V for the imperfect crystal is therefore $V_o + v(x, y, z)$, where V_o is the potential of the perfect crystal and v is the 'excess' potential due to the dopant atom. If v is small, perturbation theory can be used to express the solution to equation (4), as applied to the imperfect crystal, in terms of the corresponding solutions for a perfect crystal. Since z is linearly related to time t by the electron velocity, the 'method of variation of constants' in time-dependent perturbation theory (Bohm, 1951) is used in the analysis as described below.

In the column approximation, high-energy electron scattering is assumed to take place within only a small volume of material (Hirsch *et al.*, 1965). A dopant atom will therefore modify electron scattering only in the column centred around it (see §3.2 for a more detailed discussion of this assumption). All other columns have scattering characteristics similar to that of the perfect crystal and are unaffected by the dopant atom. The total wavefunction in these columns is a linear combination of the individual Bloch-wave solutions for a perfect crystal. Since for small perturbations the electron wavefunction in the column containing the dopant atom must be similar to that for the neighbouring 'perfect crystal' column, the perturbed wavefunction ψ' in the former column can be expressed as (Bohm, 1951)

$$\psi'(x, y, z) = \left[\sum_p \varepsilon^p(z)\varphi^p(x, y, z)\right]\exp(2\pi i k_z z), \quad (6)$$

where $\varepsilon^p(z)$ is the excitation of the pth perfect-crystal Bloch wave [*i.e.* $\varepsilon^p(x, y, z)$] at depth z. Unlike a perfect crystal, the Bloch-wave excitations are now a function of z owing to the perturbing potential of the dopant atom. Equation (6) is similar to equation (3). Hence for the imperfect crystal the term within the square brackets of equation (6) replaces φ in equation (4) with V being modified to $V_o + v(x, y, z)$. Hence we get

$$\sum_p \left(\frac{\mathrm{d}\varepsilon^p}{\mathrm{d}z} \varphi^p + \varepsilon^p \frac{\partial \varphi^p}{\partial z} \right) = \sum_p i \left[H_{\mathrm{o}} + \frac{2\pi me}{h^2 k_z} v(x, y, z) \right] \varepsilon^p \varphi^p$$

$$\text{where} \quad H_{\mathrm{o}} = \frac{\nabla_{xy}^2}{4\pi k_z} + \frac{\pi}{k_z}(k_x^2 + k_y^2) + \frac{2\pi me}{h^2 k_z} V_{\mathrm{o}}. \qquad (7)$$

Since the last term within the left-hand pair of brackets is equal to the first term within the right-hand pair of brackets in the first line of equation (7) [see equation (4)], we have after expanding the pth Bloch wave according to equation (5)

$$\sum_p \frac{\mathrm{d}\varepsilon^p}{\mathrm{d}z} b^p \exp(2\pi i \gamma^p z) = \frac{2\pi i m e}{h^2 k_z} \sum_p v(x, y, z) \varepsilon^p b^p \exp(2\pi i \gamma^p z). \qquad (8)$$

Multiplying both sides of the above equation by the complex conjugate of the qth Bloch wave [i.e. $b^{q*} \exp(-2\pi i \gamma^q z)$; the $*$ symbol denotes the complex conjugate] and integrating over the xy plane results in (Bohm, 1951)

$$\frac{\mathrm{d}\varepsilon^q(z)}{\mathrm{d}z} = \frac{2\pi i m e}{h^2 k_z} \sum_p \varepsilon^p(z) \exp[2\pi i (\gamma^p - \gamma^q) z]$$
$$\times \int b^p v(x, y, z) b^{q*} \,\mathrm{d}x \,\mathrm{d}y, \qquad (9)$$

where the orthonormal property of the Bloch waves was used to evaluate the integrals, i.e.

$$\int b^p(x, y) b^q(x, y)^* \,\mathrm{d}x \,\mathrm{d}y = \delta_{pq}, \qquad (10)$$

where δ_{pq} is the Kronecker delta.

Equation (9) represents electron scattering due to the dopant atom. In the next section, the implications of this equation are discussed and compared to the Howie–Whelan equation.

2.2. Comparison of dopant-atom scattering with the Howie–Whelan equation

The perturbation theory developed in the previous section describes electron scattering due to a change in the local electrostatic potential, while the Howie–Whelan equation is valid for the case of a slowly varying elastic strain field. It is therefore interesting at this point to compare the two forms of scattering. The Howie–Whelan equation in matrix form is (Hirsch et al., 1965)

$$\frac{\mathrm{d}\varepsilon}{\mathrm{d}z} = 2\pi i \left[\{\exp(-2\pi i \gamma^p z)\} \mathbf{C}^{-1} \{\beta_{\mathbf{g}}'\} \mathbf{C} \{\exp(2\pi i \gamma^p z)\} \right] \varepsilon, \quad (11)$$

where ε is a column matrix of the excitations of individual Bloch waves at a depth z, $\mathbf{C}$ is the matrix of Bloch-wave Fourier coefficients and the curly brackets $\{\}$ denote diagonal matrices. Furthermore, $\beta_{\mathbf{g}}' = \partial(\mathbf{g} \cdot \mathbf{R})/\partial z$, where $\mathbf{R}$ is the local displacement due to the elastic strain field. Equation (11) indicates that the excitation of a given Bloch wave q partially depends on scattering from Bloch wave p; scattering between Bloch waves from different branches of the dispersion surface (i.e. $p \neq q$) is known as interband scattering, while intraband scattering represents scattering along the same branch of the dispersion surface (i.e. $p = q$) (Hirsch et al., 1965). If $S_{qp}(z)$ represents the partial scattering contribution from Bloch wave

p to Bloch wave q at a depth z, then by evaluating the terms within the square brackets of equation (11) it is easy to show that (Nellist et al., 2008)

$$S_{qp}(z) = \varepsilon^p(z) \sum_{\mathbf{g} \neq 0} C_{\mathbf{g}}^p C_{\mathbf{g}}^q \beta_{\mathbf{g}}' \exp[2\pi i(\gamma^p - \gamma^q)z], \qquad (12)$$

where we have ignored the constant factor $2\pi i$ in equation (11).

The exponential term in equation (12) represents the phase change undergone by an electron scattered from one branch of the dispersion surface to another (Hirsch et al., 1965). This phase term is also observed for scattering by a dopant atom [equation (9)]. The magnitude of the scattering is, however, different for equations (9) and (12). In equation (9) for example, for a given Bloch-wave excitation $\varepsilon^p(z)$, the scattering magnitude is determined by the integral term; hence for scattering to be large both Bloch waves p and q must have significant amplitude at the site of the dopant atom. This means that for substitutional dopant atoms the integral has a large value for intraband scattering of the $1s$ Bloch state which channels down the atom columns. Furthermore, for a given Bloch-wave excitation, intraband scattering of the non-$1s$ states is relatively weaker and interband scattering will be predominantly between $1s$ and other Bloch states. The scattering mechanisms are, however, different for an interstitial dopant atom that does not overlap with any host atoms when the crystal is viewed in projection; here the integral is small for intraband scattering of the $1s$ state and likewise interband scattering will be predominantly between the non-$1s$ states.

In the case of elastic strain, for a given Bloch-wave excitation $\varepsilon^p(z)$ the magnitude of the scattering is determined by the Fourier coefficients of Bloch waves p and q weighted by the local deformation $\beta_{\mathbf{g}}'$ [equation (12)]. Nellist et al. (2008) have examined Bloch-wave scattering along symmetry zone axes (i.e. zone axes such as [001] and [111] in face-centred cubic and b.c.c. crystals where the main Bragg diffracted beams are related by rotational symmetry) in a non-absorbing crystal and have shown that intraband scattering is forbidden irrespective of the nature of the elastic strain field. Furthermore, interband scattering is restricted to Bloch waves that satisfy the dipole selection rule i.e. $\Delta l = \pm 1$, where l is the angular momentum quantum number assigned to a given Bloch wave (Buxton et al., 1978). Hence interband scattering can take place from an s-type Bloch state to a p-symmetry Bloch state but not to, for example, a d-symmetry Bloch state. These scattering rules have been numerically verified for the case of the Eshelby twist strain field around an end-on screw dislocation in a thin [111] b.c.c. Mo foil taking into account absorption (Mendis & Hemker, 2008).

There are hence clear differences between electron scattering from a dopant atom and an elastic strain field. Intraband scattering can be significant for the former and is forbidden along a symmetry zone axis for the latter. Furthermore, in the Howie–Whelan equation interband scattering follows the dipole selection rule for symmetry zone axes, while for a dopant atom it is largely dependent on the amplitude of the Bloch waves of interest at the site of the

dopant atom. Another important difference between the two scattering mechanisms is the fact that for an elastic strain field additional scattering rules may apply depending on the nature of $\beta'_{\mathbf{g}}$ (Hirsch *et al.*, 1965; Nellist *et al.*, 2008). For example, in two-beam conditions scattering cannot take place if the displacement **R** is perpendicular to the reciprocal-lattice vector **g**. This is, however, not the case for dopant atoms since the excess potential ν appearing in the integral term of equation (9) is to a good approximation spherically symmetric.

3. Simulations of dopant-atom scattering

3.1. Simulation procedure

Simulations are carried out for an Mo dopant atom in [001]- and [111]-oriented b.c.c. Fe. The wavevector of the incident electrons is parallel to the optic axis and the microscope
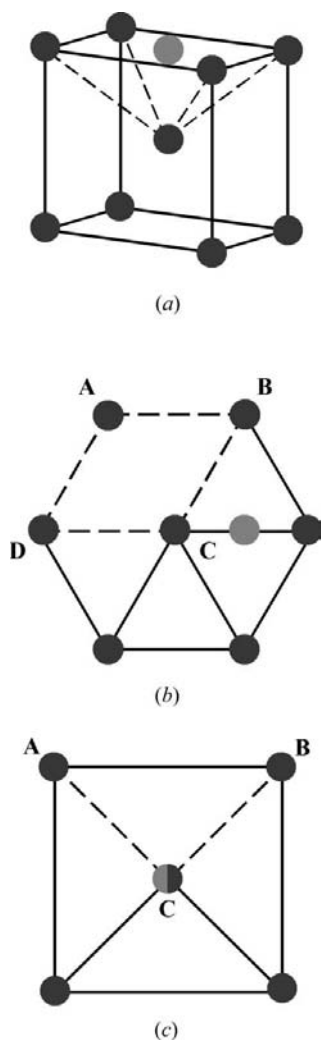

Figure 1
(*a*) Schematic showing location of a dopant atom (grey circle) in the octahedral interstice of a b.c.c. lattice. In (*b*) and (*c*) the projected position of the dopant atom is indicated for the crystal viewed along the [111] and [001] zone axes, respectively. In (*c*) the dopant atom overlaps with the central atom column of the host lattice. Regions ABCD and ABC in (*b*) and (*c*) indicate the area used for Bloch-wave normalization (see text for further details).

operating voltage is 200 kV. The dopant atom is placed at either a substitutional position or at an octahedral interstice (Fig. 1*a*). The interstitial Mo atom will directly overlap with a projected atom column of Fe in the [001] orientation (Fig. 1*c*) but not for the [111] orientation (Fig. 1*b*). For a substitutional dopant atom, the excess potential ν in equation (9) is equal to the potential difference between free atoms of Mo and Fe; for interstitial dopant atoms ν is simply the potential of a free Mo atom. The potential of an atom is determined by inverse Fourier transforming its Born-atom scattering factor (Humphreys, 1979) and the atom scattering factors of Kirkland (1998) were used for this purpose. The crystal is divided into 0.1 Å-thick slices in the z direction so that given the Bloch-wave excitations at the entrance surface of the slice the corresponding values at the exit surface can be calculated using a finite-difference method based on equation (9). This process is carried out within only 1 Å either side of the dopant atom along the z direction, since beyond 1 Å the excess potential ν is negligible and hence there can be no Bloch-wave scattering. A total of 121 Bloch waves, based on reciprocal vectors lying in the ZOLZ plane, were used for the simulations; such a large number of reciprocal vectors are required to accurately simulate Bloch-wave amplitudes. The Bloch waves must be suitably normalized so that equation (10) is satisfied. The choice of the normalizing area is somewhat arbitrary, but since we have invoked the column approximation this is chosen to be the smallest unit representing the underlying symmetry of the crystal. For a [111]-oriented b.c.c. lattice with C_3 rotational symmetry this corresponds to the parallelogram ABCD in Fig. 1(*b*), while in the [001] orientation the smallest unit is the isosceles triangle ABC in Fig. 1(*c*). Simulations are performed for dopant atoms at depths of 5 and 45 Å in a 50 Å-thick foil. At these foil thicknesses absorption is negligible and is therefore not included in the calculations.

Multislice simulations were carried out using the *Temsim* software developed by Kirkland (1998). Supercells containing a single Mo dopant atom at the centre and having dimensions in the plane of view larger than 10 Å were used to generate 256×256 pixel images. Three distinct slices represented the *ABC* stacking sequence in the [111] orientation and two distinct slices were required for the *AB* stacking sequence along [001]. The slice thickness is therefore 0.8 Å for the former orientation and 1.4 Å for the latter orientation. Absorption was not taken into account in the multislice simulations. Only spatial frequencies below 100 mrad were allowed to contribute to the final exit wave; this procedure was necessary to suppress the high spatial frequency 'noise' which is absent in experimental HREM images.

3.2. Numerical results of dopant-atom scattering

Consider first b.c.c. Fe along the [111] orientation. Only two Bloch waves are strongly excited in the perfect crystal, *i.e.* Bloch waves 1 and 4 in the dispersion surface. The former channels along the atom columns (Fig. 2*a*) while the opposite is true for the latter (Fig. 2*b*). The excitations of these two Bloch states in the perfect crystal are $\varepsilon^1 = -0.38$ and

$\varepsilon^4 = -0.92$. Dopant-atom scattering is largely governed by these two strongly excited states, since from equation (9) the magnitude of scattering from the pth Bloch state to the qth state is weighted by the excitation term $\varepsilon^p(z)$. Following equation (12), the partial scattering contribution from Bloch state p to Bloch state q at a depth z in equation (9) is given by

$$S_{qp}(z) = \varepsilon^p(z) \int b^p v(x, y, z) b^{q*} \, dx \, dy, \qquad (13)$$

where we have again ignored the physical constants outside the integral in equation (9).

Equation (13) was evaluated close to the depth of the dopant atom where the excess potential v is sharply peaked. The magnitude of S_{qp} ($p = 1, 4$) plotted as a function of the qth Bloch state for a substitutional Mo atom in [111] Fe is shown in Fig. 3(a). Intraband scattering of Bloch wave 1 (*i.e.* S_{11}) is the dominant scattering mechanism due to Bloch wave 1 being strongly localized at the dopant atom, which therefore results in a large value for the integral term in equation (13). Compare this to the case of elastic strain where intraband transitions are forbidden along the [111] symmetry zone axis (Nellist *et al.*, 2008). Bloch wave 4 channels between the atom columns but, as Fig. 3(a) indicates, for a substitutional dopant atom, will still undergo significant intraband and interband transitions, partly due to its larger excitation within the crystal. The magnitudes of interband transitions in Fig. 3(a) generally decrease as the Bloch-state index to which the transition is being made becomes larger. Fig. 3(b) shows the S_{qp} magnitudes for an interstitial Mo atom in [111] Fe plotted as a function of the qth Bloch state with $p = 1, 4$. As indicated in Fig. 1(b), the interstitial dopant atom does not overlap with any projected atom columns of the host lattice in the [111] orientation so that the S_{q1} values for Bloch wave 1 are negli-

gible. Scattering from Bloch wave 4 is however, considerably larger since this Bloch state channels between the atom columns and because the excess potential v is now equal to the full potential of the Mo atom rather than the potential difference between Mo and Fe atoms, as was the case for a substitutional dopant atom. Furthermore, Fig. 3(b) indicates that for the interstitial dopant atom interband transitions to a comparatively larger number of Bloch states can take place from Bloch wave 4.

The electron wavefunction did not undergo a significant change as it propagated through the [111] crystal containing a substitutional Mo atom (results not shown) owing to the comparatively smaller values for S_{qp} compared to an interstitial Mo atom. In Fig. 4(a) the modulus of the electron wavefunction is plotted as a function of foil depth at the site of an interstitial Mo atom in [111]-oriented b.c.c. Fe. Simulation results for Mo atoms at depths of 5 and 45 Å are presented together with the result for a perfect crystal. The foil thickness is 50 Å. In both cases the wavefunction modulus increases slightly at the dopant-atom position, but after propagating to the exit surface the modulus for the Mo atom at 5 Å depth is similar to the perfect crystal, while that for the 45 Å Mo atom is larger than the perfect crystal. Hence only the Mo atom at 45 Å depth should be visible in the final exit wave. Fig. 4(b) plots the phase of the incident electrons as a function of depth relative to the interstitial Mo atom. The phase undergoes a slight increase close to the dopant atom. This phase change is easily explained by treating the dopant atom as a weak phase object and using the physical-optics-based multislice approach to describe elastic scattering. Here the incident electron wavefunction undergoes a phase change that is proportional to the projected potential V_p of the scattering atom (Cowley &

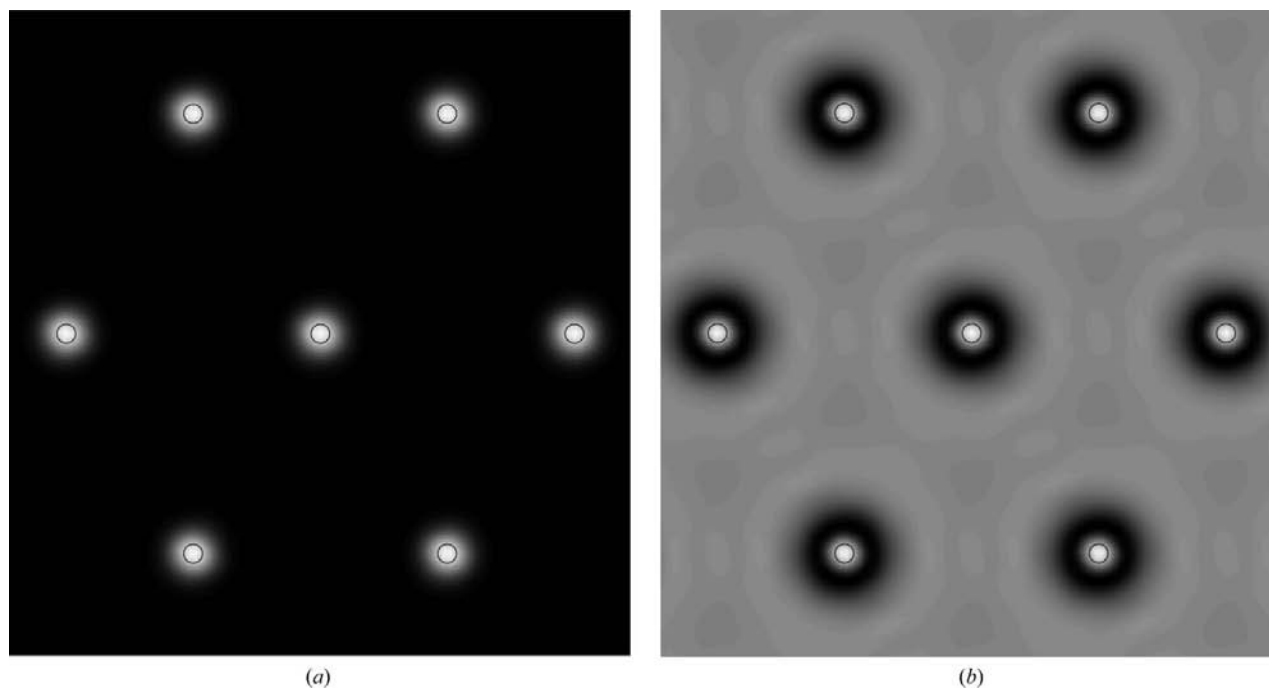(a)   (b)

Figure 2
Parts (a) and (b) are the electron intensity distributions for Bloch waves 1 and 4, respectively, in the dispersion surface of a [111]-oriented b.c.c. Fe crystal. The positions of the atom columns are marked by the open black circles.

research papers

Moodie, 1957; Kirkland, 1998). Since the projected potential of an Mo atom is higher than that of Fe, the phase should increase due to dopant-atom scattering, which is consistent with the results of Fig. 4(b). Furthermore, in the multislice approach each scattering atom emits a Hüygen wavelet, the interference of which gives rise to variations in the modulus during propagation of the electrons through the specimen. This is also consistent with the change in modulus observed in Fig. 4(a).

For an [001]-oriented b.c.c. Fe crystal only Bloch waves 1 and 5 in the dispersion surface are strongly excited (the excitations in a perfect crystal are $\varepsilon^1 = 0.46$ and $\varepsilon^5 = -0.89$). The electron intensity distributions for Bloch waves 1 and 5 are shown in Figs. 5(a) and 5(b), respectively, where it can be seen that Bloch wave 1 (Bloch wave 5) channels along (between) the atom columns. Bloch wave 1 is also found to be degenerate with Bloch wave 2, although the latter is not excited in the perfect crystal. Bloch wave 2 has an identical electron intensity distribution to Bloch wave 1 but opposite polarity. Fig. 6(a) plots the magnitude of S_{qp} ($p = 1, 5$) as a function of the qth Bloch state for a substitutional Mo atom in [001] Fe. The presence of not one but two Bloch states that are
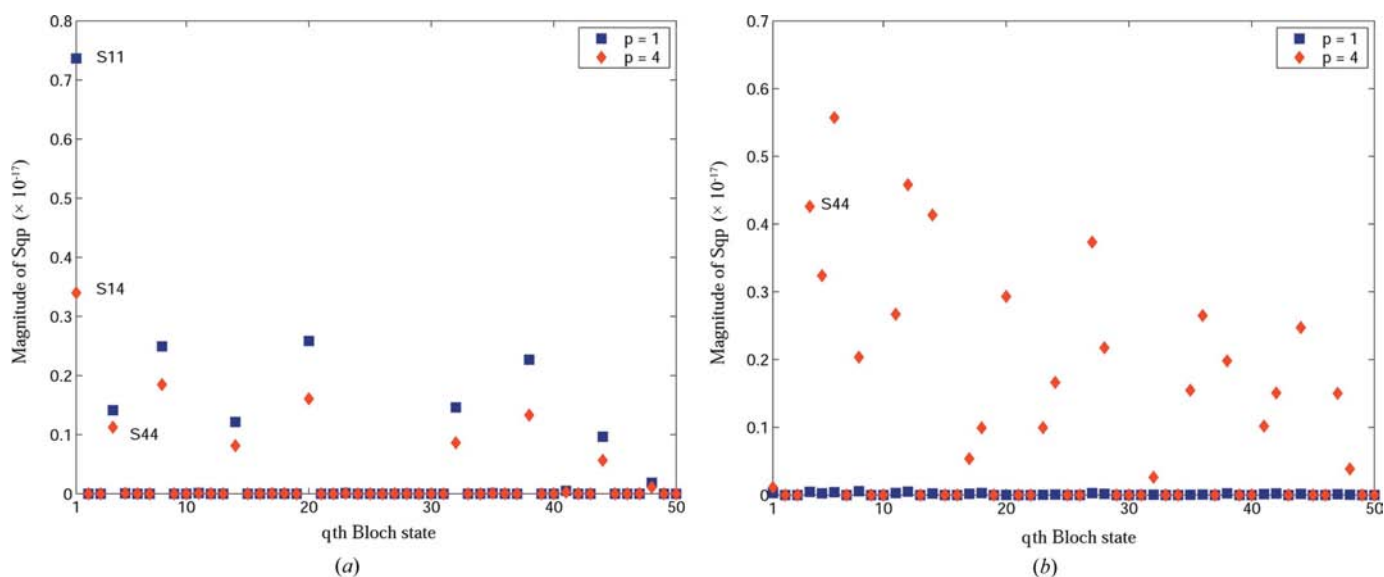

Figure 3
Magnitude of the partial scattering contribution (S_{qp}) plotted as a function of the qth Bloch state for (a) a substitutional and (b) an interstitial Mo atom in a [111]-oriented Fe crystal with $p = 1, 4$. Some of the important transitions (e.g. S_{11}, S_{44} etc.) are indicated in the figure.
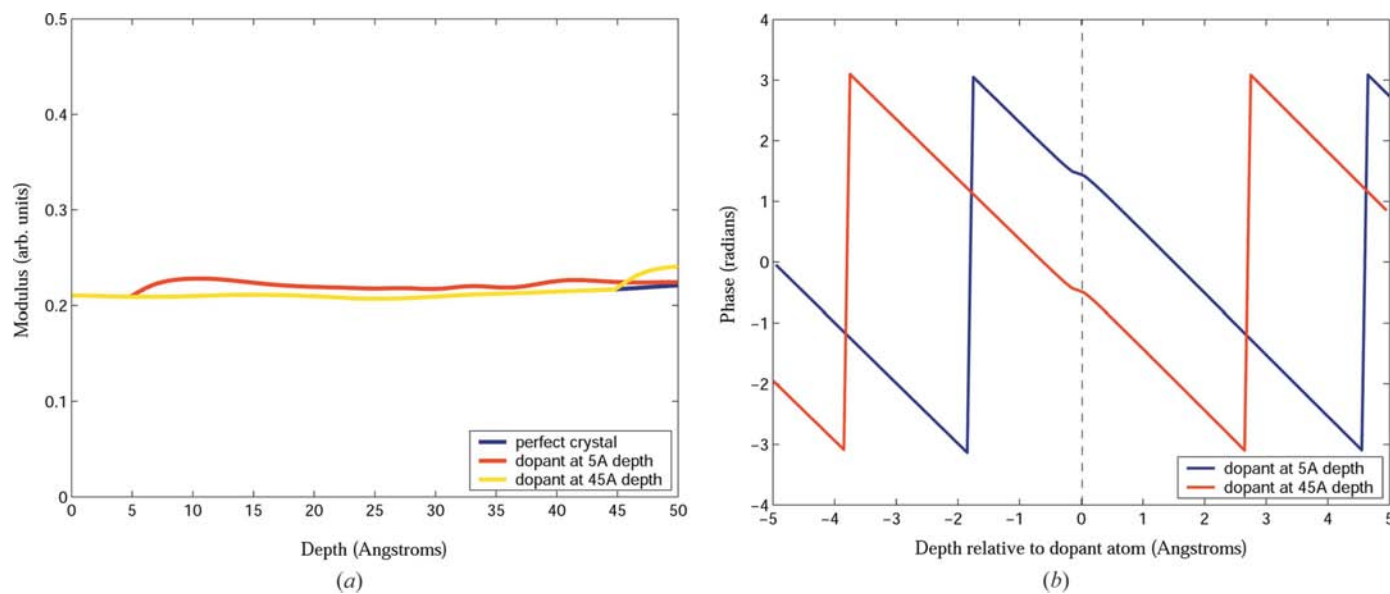

Figure 4
(a) Modulus of the electron wavefunction at the site of an interstitial Mo atom plotted as a function of depth in a 50 Å-thick [111] Fe crystal. Results for an Mo atom at depths of 5 and 45 Å are shown together with the result for a perfect crystal. In (b) the phase of the electron wavefunction is plotted as a function of depth relative to the dopant atom.

sharply peaked at the atom columns (*i.e.* Bloch waves 1 and 2) leads to more than one dominant scattering mechanism *i.e.* S_{11} (intraband scattering of Bloch wave 1) and S_{21} (interband scattering from Bloch wave 1 to Bloch wave 2). It is important to realise that this phenomenon does not require both Bloch states to have a nonzero excitation within the perfect crystal; only one Bloch state need be strongly excited. Fig. 6(*a*) also indicates that interband transitions take place from Bloch wave 1 to other Bloch states as well as interband scattering

from Bloch wave 5, although the magnitude of these transitions are significantly smaller than S_{11} and S_{21}. Fig. 6(*b*) plots the S_{qp} ($p = 1, 5$) magnitudes as a function of the qth Bloch state for an interstitial Mo atom in [001] Fe. An octahedral interstitial atom in a b.c.c. crystal directly overlaps with an atom column of the host atoms when viewed along the [001] zone axis (Fig. 1*c*). Hence for an interstitial atom the scattering mechanisms taking place are identical to those observed for a substitutional dopant atom. The magnitude of the tran-
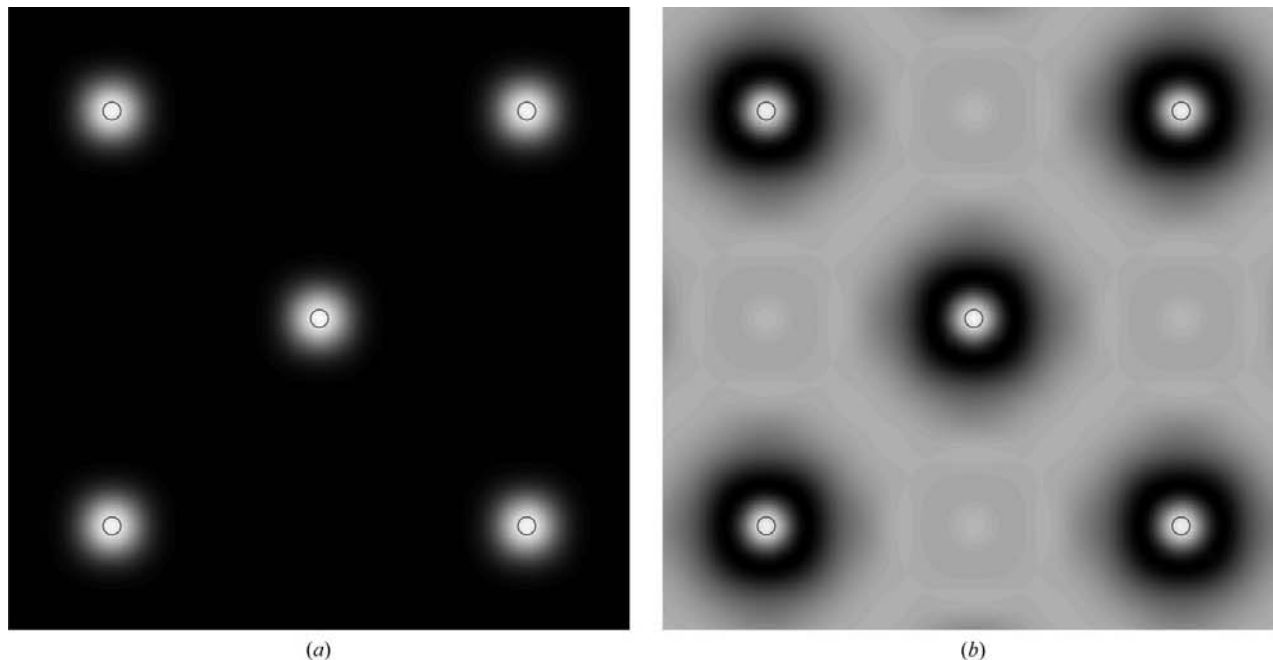

Figure 5
Parts (*a*) and (*b*) show the electron intensity distributions for Bloch waves 1 and 5, respectively, in the dispersion surface of an [001]-oriented b.c.c. Fe crystal. The positions of the atom columns are marked by the open black circles.
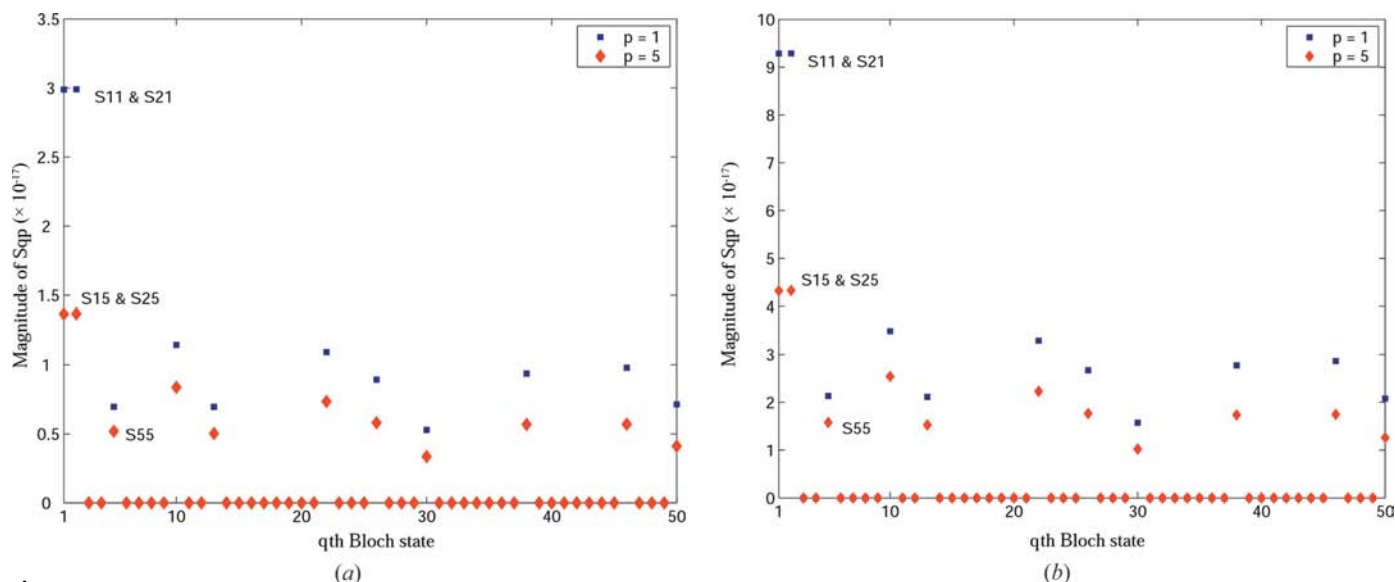

Figure 6
Magnitude of the partial scattering contribution (S_{qp}) plotted as a function of the qth Bloch state for (*a*) a substitutional and (*b*) an interstitial Mo atom in an [001]-oriented Fe crystal with $p = 1, 5$. Some of the important transitions (*e.g.* S_{11}, S_{21} *etc.*) are indicated in the figure.

sitions will, however, be significantly larger, since the excess potential ν is equal to the full potential of an Mo atom rather than the potential difference between Mo and Fe atoms. This is consistent with the results in Fig. 6(b).

Fig. 7(a) shows the modulus of the electron wavefunction plotted as a function of depth in a 50 Å-thick [001] Fe foil at the site of a substitutional Mo atom. Results are shown for Mo atoms at depths of 5 and 45 Å as well as for the perfect crystal. The modulus is seen to increase at the dopant-atom position but for the Mo atom at 5 Å (45 Å) depth the modulus at the

exit surface is less (greater) than that of the perfect crystal. Fig. 7(b) plots the phase of the electrons as a function of depth relative to the dopant atom. The phase increases at the dopant-atom position as predicted by multislice theory. Figs. 8(a) and (b) plot the modulus and phase of the electron wavefunction for a 50 Å-thick [001] Fe foil containing an interstitial Mo atom at depths of 5 and 45 Å. The results are similar to the [001] substitutional Mo atom, although the changes to the wavefunction are larger in magnitude. This is because for the [001] orientation the scattering mechanisms
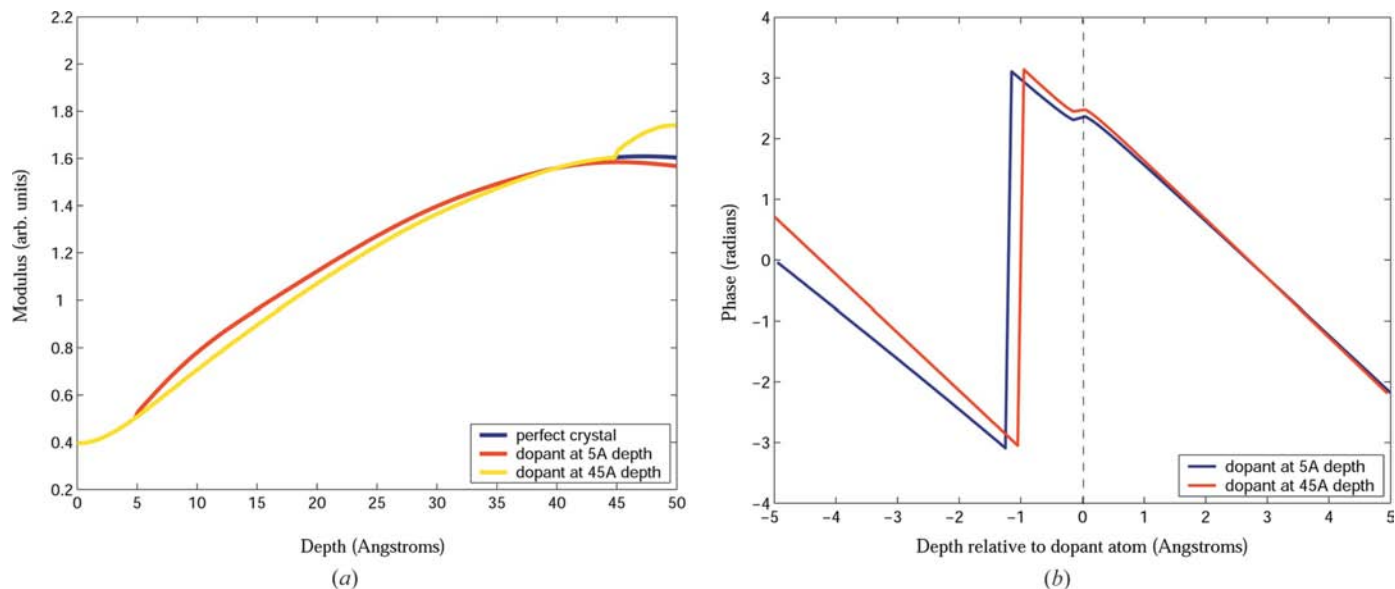

Figure 7
(a) Modulus of the electron wavefunction at the site of a substitutional Mo atom plotted as a function of depth in a 50 Å-thick [001] Fe crystal. Results for an Mo atom at depths of 5 and 45 Å are shown together with the result for a perfect crystal. In (b) the phase of the electron wavefunction is plotted as a function of depth relative to the dopant atom.
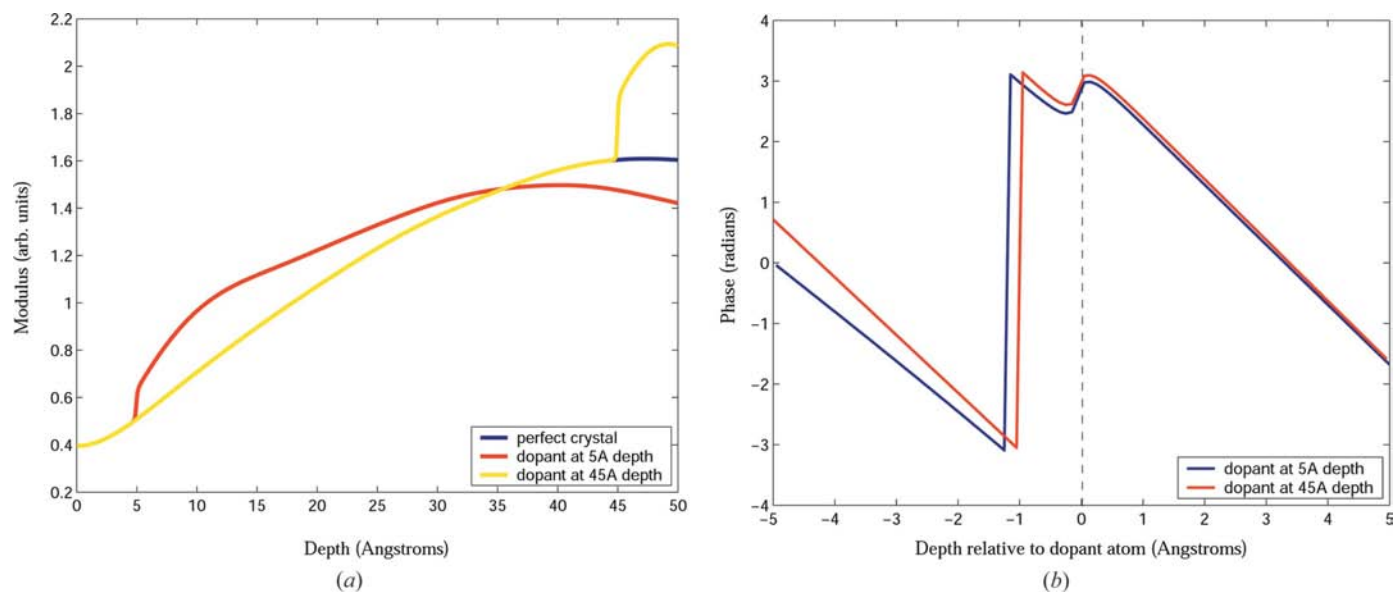

Figure 8
(a) Modulus of the electron wavefunction at the site of an interstitial Mo atom plotted as a function of depth in a 50 Å-thick [001] Fe crystal. Results for an Mo atom at depths of 5 and 45 Å are shown together with the result for a perfect crystal. In (b) the phase of the electron wavefunction is plotted as a function of depth relative to the dopant atom.

for an interstitial dopant atom are similar to a substitutional dopant atom, although the transition magnitudes are larger for the former (compare also Figs. 6a and 6b). A comparison of Figs. 4(b) and 8(b) reveals the phase increase at the interstitial dopant-atom position with respect to the perfect crystal to be ~0.1 rad in the [111] orientation and ~0.7 rad for the [001] orientation. The larger phase change in the latter orientation is due to the presence of two Bloch states that are sharply peaked at the dopant-atom position so that there are effectively two dominant scattering mechanisms. The multislice theory, however, predicts a constant phase change since the projected potential V_p is equal to that of a free Mo atom in both crystallographic orientations.

Previous theoretical work has shown that provided the slice thickness used in the multislice method is infinitesimally small (*i.e.* the so-called 'impulse limit') it is equivalent to the Bloch-wave approach for high-energy electron diffraction (Goodman & Moodie, 1974; Gratias & Portier, 1983). For dopant-atom scattering the Bloch-wave model should therefore have predicted a phase change that is independent of the crystallographic orientation. The model is only strictly valid for small perturbations but repeating the calculations for an interstitial dopant atom with smaller 'excess' potential will not remove this discrepancy, since from the previous discussion it has its origins in the magnitude and number of dominant scattering mechanisms operating in the [001] *versus* [111] b.c.c. crystallographic orientations. It is therefore important to examine the assumptions made in the Bloch-wave perturbation model more closely. First there is the neglect of higher-order Laue zone (HOLZ) reflections in deriving equation (5). HOLZ reflections will be more important for the [001] orientation compared to [111] due to a smaller HOLZ ring radius for the former (Spence & Zuo, 1992) and could therefore be a contributing factor to the discrepancy. The second and perhaps more critical assumption is the use of the column approximation. Here there are two factors that need to be considered: (i) the 'sideways' scattering of the Bragg beams that defines the column width and (ii) the magnitude of elastic diffuse scattering from the defect. For the first the Bragg angle (θ_B) for $g = 110$ diffraction in b.c.c. Fe at 200 kV is ~6 mrad. If Bragg diffraction took place at the entrance surface then, provided the foil thickness t is less than half the extinction distance, the beam would have diverged laterally by a distance of ~$2\theta_B t$ before leaving the foil. For the 50 Å-thick foils used in this study this corresponds to a distance of ~0.6 Å and is much smaller than the nearest-neighbour-atom column spacings along the [001] and [111] crystal orientations. Higher-order Bragg beams will lead to a larger lateral spreading but the intensity of these beams in a thin foil are significantly smaller compared to the $g = 110$ beams. Hence as a first approximation it is reasonable to assume that, given the simulation conditions, dopant-atom scattering is largely unaffected by the neighbouring atom columns.

Use of the column approximation, however, does mean that elastic diffuse scattering is not taken into account. Here diffuse scattering refers to the intensity transferred between the Bragg peaks due to defects in an otherwise perfect crystal.

In elastic diffuse scattering, Bloch-state transitions undergo a change in the transverse wavevector component (k_t) with respect to that of the incident beam electrons; the more localized the defect the greater the possibility of inducing transitions with large changes in k_t (Howie & Basinski, 1968). Furthermore, localized defects can also induce transitions with large changes in the longitudinal wavevector component, thereby potentially enhancing the role of HOLZ reflections on the final electron wavefunction (Howie & Basinski, 1968). In weak-beam images of dislocations for example, elastic diffuse scattering can lead to a significant shift in the image intensity peak with respect to the true dislocation core position (Howie & Sworn, 1970). For a localized defect such as a dopant atom, Bloch-state transitions with large changes in k_t are involved but due to the weak perturbing potential of a single dopant atom the magnitudes of the transitions are significantly smaller compared to (say) a dislocation core. The column approximation only takes into account those transitions where k_t is unchanged and equal to that of the incident electron beam. If the magnitudes of these transitions are large compared to the elastic diffuse scattering, then the error involved in applying the column approximation will be relatively small. In the next section it will be shown that the Bloch-wave perturbation model, which applies the column approximation to a single dopant atom, gives results that are *qualitatively* consistent with the more accurate multislice simulations. Nevertheless, the subtle phase discrepancy noted above indicates that the Bloch-wave results are *quantitatively* inaccurate. It is worth mentioning, however, that the advantage of Bloch waves over multislice simulations is the physical insight it provides into dopant-atom scattering.

3.3. Comparison with multislice simulations

In this section, the Bloch-wave results presented earlier are compared with multislice simulations. Figs. 9(a) and 9(b) show the (multislice-simulated) square modulus of the electron exit wave for a 50 Å-thick [111] Fe foil containing an interstitial Mo atom at depths of 4 and 46 Å, respectively (the depths of the dopant atoms deviate slightly from the nominal values of 5 and 45 Å due to the discrete nature of the multislice method). As predicted by the Bloch-wave calculations (see Fig. 4a), the interstitial Mo atom is visible in Fig. 9(b) but not in Fig. 9(a). Figs. 10(a)/(c) show the (multislice-simulated) square modulus of the electron exit wave for a 50 Å-thick [001] Fe foil containing a substitutional/interstitial Mo atom at 6 Å/4 Å depth. The dopant-atom position is indicated by the arrows in the figure. The square modulus within the region highlighted by the rectangular box in Fig. 10(a)/(c) is shown in Fig. 10(b)/(d). The atom column containing the dopant atom has a smaller modulus compared to its neighbouring columns. This decrease in modulus is significant for the interstitial Mo atom (Fig. 10d) but less noticeable for a substitutional Mo atom (Fig. 10b). Similarly, Figs. 10(e)–(h) indicate that dopant atoms closer to the exit surface of a 50 Å-thick [001] Fe foil have a higher modulus than the atom columns of a perfect crystal, with the effect being more evident for an interstitial atom.

These observations are consistent with Figs. 7(a) and 8(a) and confirm the general validity of the Bloch-wave model.

4. Summary and conclusions

Perturbation theory was used to develop a Bloch-wave model that describes electron scattering by a dopant atom. The electron wavefunction in the crystal containing the dopant atom is expressed as a linear combination of perfect crystal Bloch states, with the excitation of each Bloch state being determined by the elastic scattering. Scattering from one Bloch state to another partly depends on the amplitude of each Bloch state at the site of the dopant atom. Hence the scattering mechanisms will depend on whether the dopant atom is substitutional or interstitial as well as the orientation of the crystal. The scattering equation for a dopant atom was compared to the Howie–Whelan equation, which is applicable to scattering from a slowly varying elastic strain field. Important differences between the two are observed; for example, intraband transitions along symmetry zone axes are allowed for dopant atoms and, unlike elastic strain fields, there are no extinction rules. The Bloch-wave model was used to calculate the electron wavefunction for interstitial/substitutional Mo atoms in a b.c.c. Fe crystal along the [111] and [001] zone axes. The results are in general agreement with multislice simulations, although subtle differences do exist. For example, the Bloch-wave model predicts the phase change of the electrons (with respect to the perfect crystal) due to scattering by the dopant atom to vary with the crystallographic orientation, although in multislice theory the phase change is constant.

This discrepancy is likely to be due to the assumptions made in the Bloch-wave model, such as the absence of a HOLZ contribution and, in particular, neglecting the effects of elastic diffuse scattering.

In many materials systems, changes to the local crystal strain and chemistry can take place simultaneously. Examples include interstitial/vacancy dislocation loops and vacancy clusters, as well as Suzuki segregation to stacking faults (Mendis et al., 2004) and Cottrell segregation to dislocations (Cadel et al., 2000). Traditionally, the image contrast of these defects has been explained by examining scattering from the elastic strain field only, but it would be interesting to estimate the contribution from the change in chemistry as well. In principle, the perturbation theory described in this paper could combine the effects of elastic strain field and chemistry into one unified model of Bloch-wave scattering. The excess potential v would then be due to the change in chemistry as well as the shift in atomic positions caused by the local deformation. This is in some ways similar to the suggestion made by Howie & Basinski (1968) of using a crystal potential based on the rigid-ion approximation to take account of both strain and structure-factor contrast simultaneously. It should be noted, however, than any perturbation model is only an approximation and it is important to carry out multislice simulations to test its accuracy. Nevertheless, much physical insight into electron-beam scattering is gained by using Bloch-wave methods. Finally, it is also possible to develop a STEM imaging theory of dopant atoms by applying the Bloch-wave model to each partial plane wave within the electron probe separately. Bloch waves have been used previously in STEM
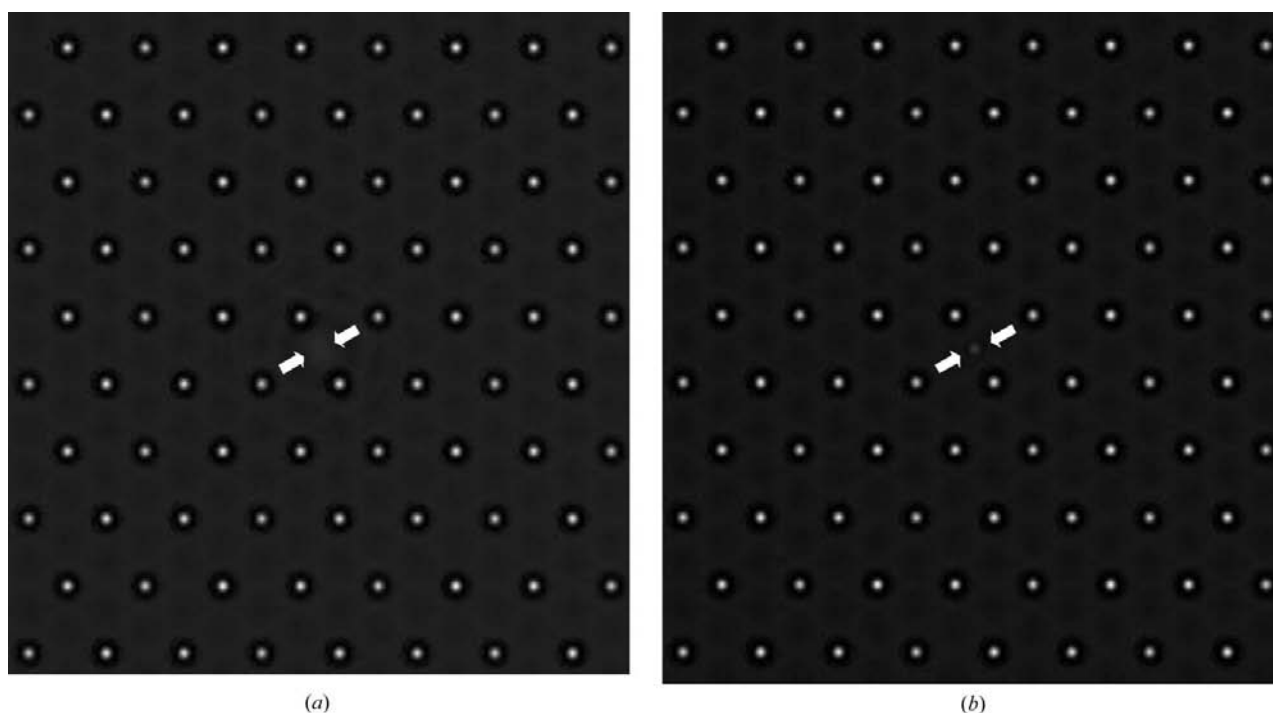

(a)

(b)

Figure 9
Multislice-simulated square modulus of the electron exit wave for a 50 Å-thick [111] Fe crystal containing an interstitial Mo atom at depths of (a) 4 Å and (b) 46 Å. The position of the Mo atom is indicated by the arrows in each figure.
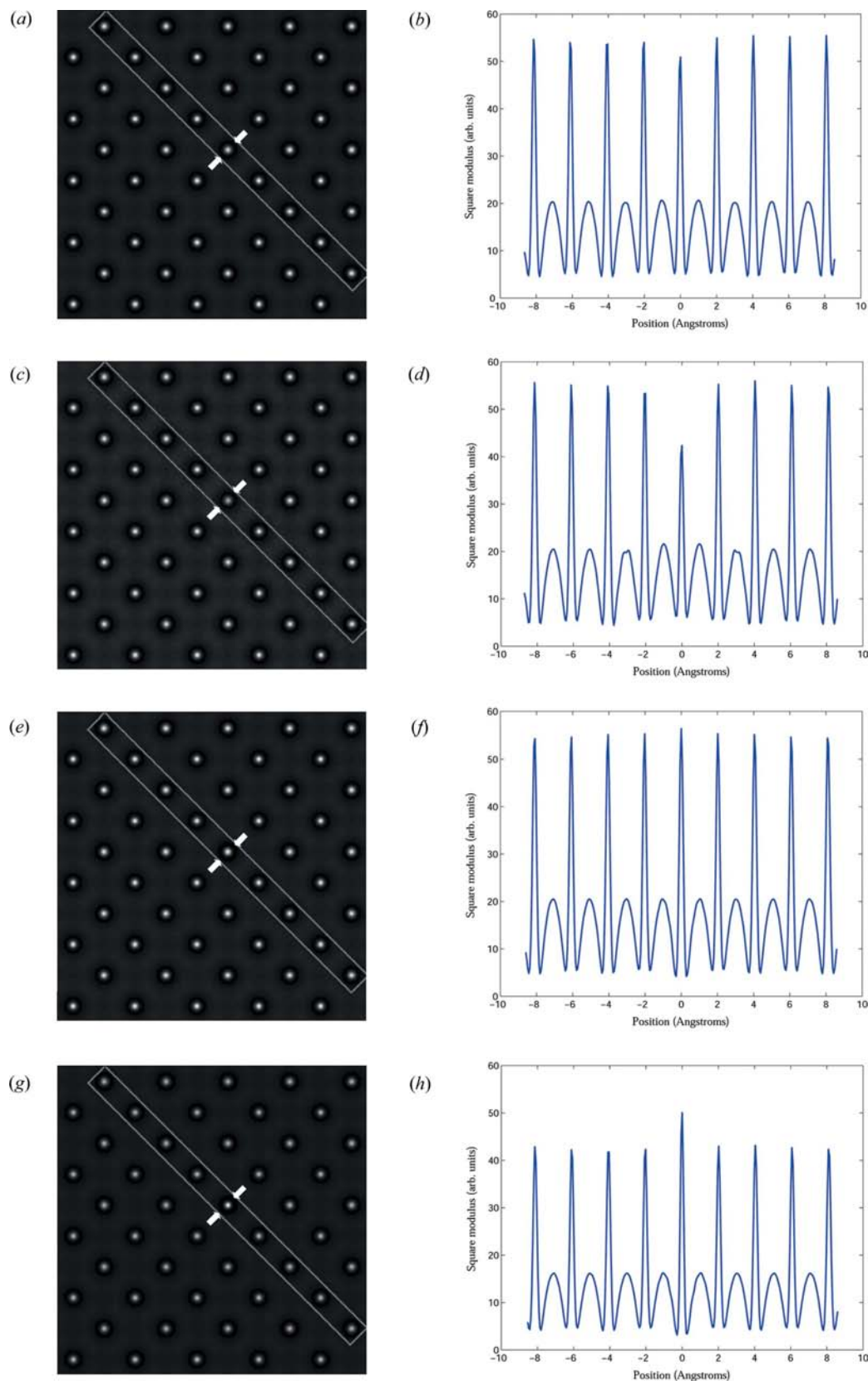
Figure 10
Multislice-simulated square modulus of the electron exit wave for a 50 Å-thick [001] Fe crystal containing (*a*) a substitutional Mo atom at 6 Å depth, (*c*) an interstitial Mo atom at 4 Å depth, (*e*) a substitutional Mo atom at 44 Å depth and (*g*) an interstitial Mo atom at 47 Å depth. The atom column containing the Mo atom is indicated by the arrows in each figure. The rectangular box in each figure represents the region from which the square modulus was extracted. Line traces of the square modulus for (*a*), (*c*), (*e*) and (*g*) are shown in (*b*), (*d*), (*f*) and (*h*), respectively. The atom column containing the Mo atom is arbitrarily placed at 0 Å.

calculations but have been restricted to perfect crystals (Pennycook & Jesson, 1991; Nellist & Pennycook, 1999; Allen *et al.*, 2003; Findlay *et al.*, 2003). In an incoherent imaging technique such as HAADF, the signal from a given atom is proportional to the local electron intensity (*i.e.* the square modulus of the electron wavefunction at that position). The Bloch-wave perturbation method could therefore be used to understand how dopant-atom scattering would modify the electron wavefunction and thereby deduce its effect on dopant-atom contrast as well as optical sectioning experiments. This will be the subject of a separate paper.

References

Allen, J. E., Hemesath, E. R., Perea, D. E., Lensch-Falk, J. L., Li, Z. Y., Yin, F., Gass, M. H., Wang, P., Bleloch, A. L., Palmer, R. E. & Lauhon, L. J. (2008). *Nature Nanotech.* **3**, 168–173.

Allen, L. J., Findlay, S. D., Oxley, M. P. & Rossouw, C. J. (2003). *Ultramicroscopy*, **96**, 47–63.

Benthem, K. van, Lupini, A. R., Kim, M., Baik, H. S., Doh, S. J., Lee, J.-H., Oxley, M. P., Findlay, S. D., Allen, L. J. & Pennycook, S. J. (2005). *Appl. Phys. Lett.* **87**, 034104-1–034104-3.

Bohm, D. (1951). *Quantum Theory*. New York: Prentice-Hall.

Buxton, B. F., Loveluck, J. E. & Steeds, J. W. (1978). *Philos. Mag. A*, **38**, 259–278.

Cadel, E., Launois, S., Fraczkiewicz, A. & Blavette, D. (2000). *Philos. Mag. Lett.* **80**, 725–736.

Cowley, J. M. (1988). *High-Resolution Transmission Electron Microscopy and Associated Techniques*, edited by P. R. Buseck, J. M. Cowley & L. Eyring. Oxford University Press.

Cowley, J. M. & Moodie, A. F. (1957). *Acta Cryst.* **10**, 609–619.

Findlay, S. D., Allen, L. J., Oxley, M. P. & Rossouw, C. J. (2003). *Ultramicroscopy*, **96**, 65–81.

Goodman, P. & Moodie, A. F. (1974). *Acta Cryst.* A**30**, 280–290.

Gratias, D. & Portier, R. (1983). *Acta Cryst.* A**39**, 576–584.

Hirsch, P. B., Howie, A., Nicholson, R. B., Pashley, D. W. & Whelan, M. J. (1965). *Electron Microscopy of Thin Crystals*. Washington: Butterworths.

Howie, A. & Basinski, Z. S. (1968). *Philos. Mag.* **17**, 1039–1063.

Howie, A. & Sworn, C. H. (1970). *Philos. Mag.* **22**, 861–864.

Humphreys, C. J. (1979). *Rep. Prog. Phys.* **42**, 1825–1887.

Jia, C. L., Lentzen, M. & Urban, K. (2003). *Science*, **299**, 870–873.

Jones, I. P. (2002). *Adv. Imaging Electron Phys.* **125**, 63–117.

Kirkland, E. J. (1998). *Advanced Computing in Electron Microscopy*. New York: Plenum Press.

Loane, R. F., Kirkland, E. J. & Silcox, J. (1988). *Acta Cryst.* A**44**, 912–927.

Mendis, B. G. & Hemker, K. J. (2007). *Philos. Mag.* **87**, 4229–4251.

Mendis, B. G. & Hemker, K. J. (2008). *Ultramicroscopy*, **108**, 855–864.

Mendis, B. G., Jones, I. P. & Smallman, R. E. (2004). *J. Electron Microsc.* **53**, 311–323.

Nellist, P. D., Cosgriff, E. C., Hirsch, P. B. & Cockayne, D. J. H. (2008). *Philos. Mag.* **88**, 135–143.

Nellist, P. D. & Pennycook, S. J. (1996). *Science*, **274**, 413–415.

Nellist, P. D. & Pennycook, S. J. (1999). *Ultramicroscopy*, **78**, 111–124.

Pennycook, S. J. & Jesson, D. E. (1991). *Ultramicroscopy*, **37**, 14–38.

Sarosi, P. M., Hriljac, J. A. & Jones, I. P. (2003). *Philos. Mag.* **83**, 4031–4044.

Shannon, M. D., Lok, C. M. & Casci, J. L. (2007). *J. Catal.* **249**, 41–51.

Shibata, N., Pennycook, S. J., Gosnell, T. R., Painter, G. S., Shelton, W. A. & Becher, P. F. (2004). *Nature (London)*, **428**, 730–733.

Spence, J. C. H. & Taftø, J. (1983). *J. Microsc.* **130**, 147–154.

Spence, J. C. H. & Zuo, J. M. (1992). *Electron Microdiffraction*. New York: Plenum Press.

Suenaga, K., Tencé, M., Mory, C., Colliex, C., Kato, H., Okazaki, T., Shinohara, H., Hirahara, K., Bandow, S. & Iijima, S. (2000). *Science*, **290**, 2280–2282.

Voyles, P. M., Grazul, J. L. & Muller, D. A. (2003). *Ultramicroscopy*, **96**, 251–273.

Voyles, P. M., Muller, D. A., Grazul, J. L., Citrin, P. H. & Gossmann, H.-J. L. (2002). *Nature (London)*, **416**, 826–829.

Voyles, P. M., Muller, D. A. & Kirkland, E. J. (2004). *Microsc. Microanal.* **10**, 291–300.

Wilkens, M. (1964). *Phys. Status Solidi*, **6**, 939–956.